Influence of shock waves on laser-driven proton acceleration

O. Lundh, F. Lindau, A. Persson, and C.-G. Wahlström
Department of Physics, Lund University, P.O. Box 118, S-22100 Lund, Sweden

P. McKenna
SUPA, Department of Physics, University of Strathclyde, Glasgow G4 0NG, United Kingdom

D. Batani
Dipartimento di Fisica, Università di Milano Bicocca, Piazza della Scienza 3, 20126 Milano, Italy
(Received 3 May 2007; published 28 August 2007)

The influence of shock waves, driven by amplified spontaneous emission (ASE), on laser-accelerated proton beams is investigated. A local deformation, produced by a cold shock wave launched by the ablation pressure of the ASE pedestal, can under oblique laser irradiation significantly direct the proton beam toward the laser axis. This can be understood in the frame of target normal sheath acceleration as proton emission from an area of the target where the local target normal is shifted toward the laser axis. Hydrodynamic simulations and experimental data show that there exists a window in laser and target parameter space where the target can be significantly deformed and yet facilitate efficient proton acceleration. The dependence of the magnitude of the deflection on target material, foil thickness, and ASE pedestal intensity and duration is experimentally investigated. The deflection angle is found to increase with increasing ASE intensity and duration and decrease with increasing target thickness. In a comparison between aluminum and copper target foils, aluminum is found to yield a larger proton beam deflection. An analytic model is successfully used to predict the proton emission direction.

DOI: 10.1103/PhysRevE.76.026404 PACS number(s): 52.38.Kd, 52.35.Tc, 52.38.Mf, 29.27.Fh

I. INTRODUCTION

Laser-driven proton and heavy ion acceleration is an area of research that currently attracts significant scientific interest. The particle beams produced in these experiments have a number of attractive characteristics, such as high laser to particle beam conversion efficiency [1], very low emittance [2], and a small virtual source size [3]. Proposed applications of this possibly compact ion beam source include ion radiotherapy for cancer treatment [4], isotope production for medical imaging techniques [5], and injectors for future ion accelerators [6]. These applications have different requirements with regards to ion energy, conversion efficiency, and beam quality and, before they can be realized, a better understanding of the underlying processes must be established so that the ion beam can be appropriately optimized.

In a typical experiment, a high power laser pulse is tightly focused on the surface of a thin foil to an intensity exceeding 10^{19} W/cm^2. The laser interacts preferentially with plasma electrons (to accelerate ions directly requires higher intensities than are currently available) and, according to a number of different mechanisms, a population of hot electrons with a Maxwellian temperature of typically a few MeV is generated. These electrons traverse the target and build up exceptionally high electrostatic fields ($\sim$TV/m) at the surfaces of the foil. Atoms on the target surface experience the field and are rapidly field-ionized and accelerated. The magnitude of the electric field depends on the electron temperature and density. For a given laser pulse it is possible to increase the hot electron density on the rear surface of the target by decreasing the foil thickness. This minimizes the geometrical spreading of the electron beam during the transport through the target and consequently the highest proton energies and the highest conversion efficiencies are reached by using very thin foils [1]. However, there are limits as to how thin foils can be used in order to optimize the proton beam. The most severely limiting factor in experiments is the fact that, due to the large gain in the laser system and amplified spontaneous emission (ASE) in the amplifiers, a nanosecond pedestal precedes the main pulse. When focused, this pedestal can become so intense that it significantly changes the properties of the target prior to the main pulse arrival. The effects induced by the ASE pedestal varies with intensity. Even at a relatively low intensity ($\sim 10^{10}$ W/cm^2), material at the target front surface is evaporated and partially ionized prior to the main pulse arrival. As this preplasma expands into vacuum, the initially sharp target density profile is smoothed on the front of the foil. This has important implications for the mechanisms of proton acceleration. In fact, it has been shown theoretically and experimentally that the acceleration is most effective for a steep ion density gradient, whereas a long ion density scale length severely limits the maximum proton energy [7,8]. The presence of a preplasma at the front of the target might therefore explain why the most energetic protons have been observed to originate from the rear surface of the foil [9]. At medium ASE intensities ($\sim 10^{12}$ W/cm^2) not only the front but also the bulk of the target is significantly influenced. The preplasma has in this case such a high temperature that the front side plasma expansion launches a compressional shock wave into the target. Given enough time, it will break through the rear surface of the foil and significantly influence the properties of the proton emitting region [10–13]. At even higher ASE intensities ($>10^{13}$ W/cm^2), the shock is strong enough to induce phase

transitions and even evaporate the target material. After shock breakout, this effect might create a long ion density scale length also at the rear surface, thereby terminating the proton acceleration. To avoid this and to eliminate other rear surface effects, most experimenters choose the foil thickness so that the shock front is still inside the target when the main pulse arrives.

In this article, we present a study of laser-driven proton acceleration under conditions where the ASE pedestal strongly influences the acceleration mechanisms. Between the region in laser and target parameter space where the shock has no time to break out and the region where the shock breakout ruins the steep density gradient at the rear surface, we identify a region where the shock is strong enough to significantly deform the rear surface, but yet not strong enough to terminate the proton emission. We further show that this effect can be used to manipulate the beam direction, and discuss its potentials for optical target manipulation and beam focusing.

The paper is organized as follows. In Sec. II we discuss the generation, propagation, and breakout of ASE-driven shocks and, in particular, the dependencies on target material and laser intensity. In Sec. III we describe the experimental setup and methods used for proton acceleration and how we control the ASE duration and intensity. We present the experimental results and discuss these with respect to analytical and numerical predictions in Sec. IV. Finally, in Sec. V we conclude.

II. INFLUENCE OF ASE-DRIVEN SHOCK WAVES

In this section, we discuss how ASE-driven shock waves change the properties of a thin foil target prior to the main interaction. Our discussion is based on analytical calculations and hydrodynamic simulations using the code MULTI [14], assuming a rectangular ASE temporal pulse shape.

A. Shock propagation and breakout

Figure 1 shows the result of a one-dimensional (1D) hydrodynamic simulation of the interaction between a 3 ns long ASE pedestal of medium intensity (1×10^{12} W/cm^2) and a 6 μm thick aluminum foil target. The laser hits the target at time zero and heats the plasma formed on the front side of the foil. The heated plasma expands out into the vacuum and in doing so it exerts a 30 GPa (0.3 Mbar) pressure on the remaining target. Because of this rocket effect, a shock is launched into the target. The shock wave moves with a constant velocity until it reaches the rear surface where shock breakout occurs. The rear surface then starts to expand while a rarefaction wave is backscattered into the target. The laser continues to push on the front side so the net effect is that, after shock breakout, the target is moving with a speed of typically a few μm/ns.

The scaling of the induced pressure with laser intensity has been shown to be relatively insensitive to target material [15] and can be approximated as [16]

$$P = \zeta I^{2/3}, \tag{1}$$

where the pressure P is in Pa and intensity I in W/m^2. ζ is a material specific constant which is, for a laser wavelength of

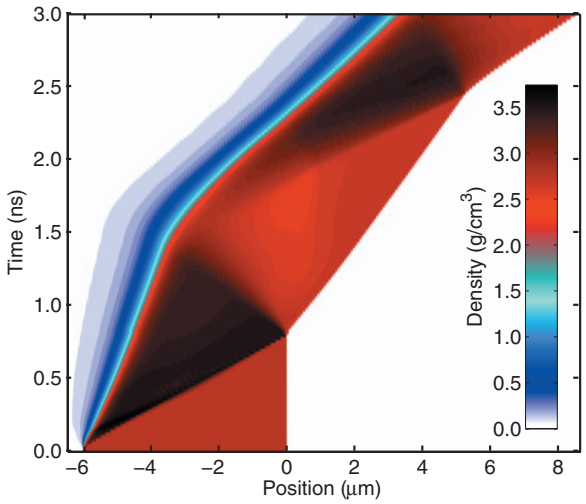

FIG. 1. (Color online) Time evolution of the density of a 6 μm aluminum target shocked by laser pulse with a constant intensity of 1×10^{12} W/cm^2. Laser ablation launches a shock at the target front which propagates inside the target at a constant speed of 7.8 μm/ns. Behind the shock front, the target is compressed to 1.4 times the initial density. The shock breaks through the rear surface 0.8 ns after the laser hit the target front and the rear surface then starts to expand with a velocity of 3.1 μm/ns, while a rarefaction wave is backscattered into the target.

0.8 μm, close to unity. For a shocked material, initially at rest, the state behind the shock front is governed by the mass and momentum conservation laws, and by an experimentally validated linear relationship between the shock and particle velocities, v_s and v_p,

$$\rho_0 v_s = \rho(v_s - v_p), \tag{2a}$$

$$P = \rho_0 v_s v_p, \tag{2b}$$

$$v_s = c_0 + \alpha v_p, \tag{2c}$$

where ρ_0 and ρ are the densities of the unperturbed and compressed material, respectively, P is the shock pressure, c_0 is the sound velocity, and α is an empirical material constant [17]. Table I gives experimental values of c_0 and α for some typical target materials, common in proton acceleration experiments. Solving Eqs. (2a)–(2c) gives the particle and shock velocities,

$$v_s = \frac{c_0}{2}(\sqrt{1+x}+1), \tag{3a}$$

$$v_p = \frac{c_0}{2\alpha}(\sqrt{1+x}-1), \tag{3b}$$

where $x=(4\alpha/\rho_0 c_0^2)P$. When the shock breaks through, the rear surface starts to expand with a velocity $v_{\exp}=2v_p$. This relation is appropriate for relatively weak shocks, i.e., when no phase transitions are induced. Figure 2 shows the position of the shock front inside a 6 μm target and the position of the rear surface after shock breakout. Assuming $\zeta=1.0$ and 0.75 J$^{1/3}$s$^{2/3}$m$^{-5/3}$ in Cu and Al, respectively, gives good

TABLE I. Experimental values [17,18] of c_0 and α for common proton acceleration target materials with initial density ρ_0 and atomic number Z. P_m is the pressure required for melting along the Hugoniot and T_m is the associated temperature [19–23].

Element	Z	ρ_0 (g/cm^3)	c_0 (μm/ns)	α	P_m (GPa)	T_m (K)
Al	13	2.70	5.24	1.40	170	5700
Ti	22	4.53	4.91	1.02		
Fe	26	7.86	3.77	1.65	260	6100
Cu	29	8.93	3.94	1.49	270	5600
Pd	46	11.99	4.01	1.55	265	5800
Sn	50	7.29	2.59	1.49	49	1300
Au	79	19.30	3.08	1.56	280	
Mylar		0.92	2.76	1.59		

agreement between simulation data and analytical calculations. As expected, the shock travels faster through Al than through Cu and reaches the rear surface at earlier times. After breakout, the expansion velocity is also higher for Al than for Cu. Therefore, for a given laser intensity, an Al target is always more affected than a Cu target.

B. Induced phase transitions

An important observation from the simulation in Fig. 1 is that, at the rear surface of the foil, the target surface-to-vacuum boundary remains sharp after the shock breakout. In contrast, simulations at higher laser intensities, shown in Fig. 3, confirm that shock breakout can result in a destruction of the sharp density gradient. A key point, when discussing proton acceleration from shocked targets, is therefore that it has been established, both theoretically and in experiments, that the proton energy is highest for sharp target boundaries [7,8]. So, to achieve efficient rear surface acceleration from a shocked target, the shock driving laser intensity needs to be adjusted to produce a relatively cold, plastic deformation. Figure 4 shows how the melting point of aluminum and copper increases as the pressure increases. When a material is compressed by a shock, the state of the compressed material is described by the Hugoniot curve, also shown in Fig. 4. Note that this curve does not show a transition trajectory of the material as the pressure is being ramped, but rather the final state behind the front of a shock of a certain pressure. The intersection of the melting curve and the Hugoniot curve gives the pressure required for shock melting. In combina-

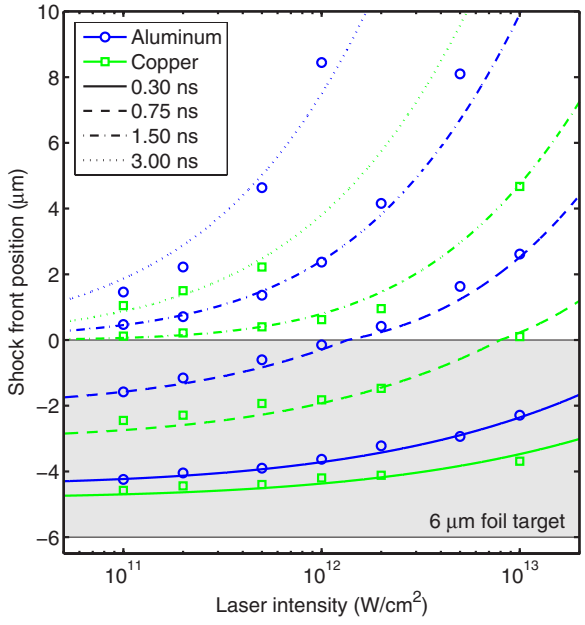

FIG. 2. (Color online) Shock front position inside a 6 μm target and the position of the rear surface after breakout. Simulation results (symbols) are in reasonably good agreement with analytical calculations (lines). The shock speed is increasing with laser intensity, but is lower in Cu than in Al.

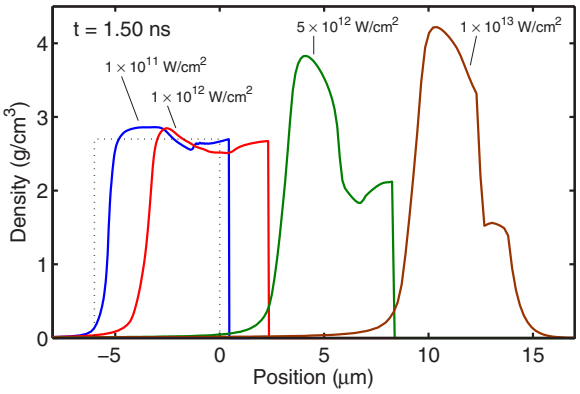

FIG. 3. (Color online) Density profile of a 6 μm thick aluminum target after 1.5 ns for different laser intensities. The dotted line shows the unperturbed density profile. At 1×10^{12} W/cm^2, laser ablation generates a relatively cold and plastic deformation of the target. Increasing the intensity one order of magnitude heats the shocked material and creates a density ramp at the rear surface. Such a ramp has been shown to decrease the maximum proton energy.

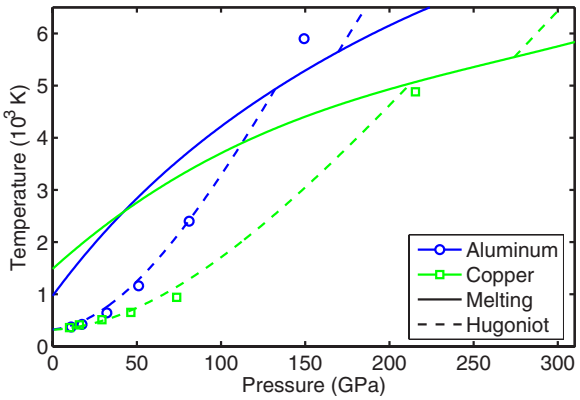

FIG. 4. (Color online) Temperature just behind the shock front in the center of a 6 μm target, obtained using the code MULTI. The simulation data (symbols) compares well with the shock-release model (dashed), proposed by Dai *et al.* [19], for assessing the melting on Hugoniots of metals. The intersection of the melting (solid) and Hugoniot (dashed) curves gives an estimate of the pressure below which the shocked target is in a solid phase.

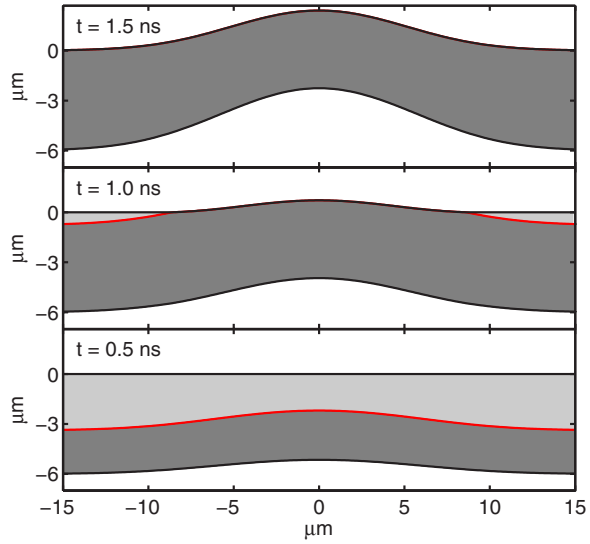

FIG. 5. (Color online) Analytical calculation of the propagation and breakout of a shock wave, driven in a 6 μm aluminum target by a 1×10^{12} W/cm^2 ASE pedestal, with a 10 μm (FWHM) Gaussian focal spot. The dark gray area between the shock front and the ablation front is the compressed target. The degree of compression varies along the radial coordinate and is a consequence of different shock pressure. Not shown is the low density coronal plasma in the lower white region that drives the shock wave.

tion with the intensity-pressure relation in Eq. (1), this gives an estimate of the laser intensity below which the shock produces a plastic deformation with a sharp rear surface density gradient, facilitating efficient ion acceleration.

C. Two-dimensional effects

So far we have only considered the propagation of a planar (1D) shock. In reality, the ASE intensity varies over the focal region so that the highest shock pressure, and consequently the largest rear surface deformation, occurs in the center of the focus. Important for proton acceleration is the geometrical shape of the target foil. To model the time dependent shape, we assume that the shock pressure depends only on the local intensity and that the lateral shock spreading can be neglected. This assumption is realistic for relatively thin targets as compared to the focal spot diameter. Assuming a Gaussian laser intensity distribution and using Eqs. (1), (2a)–(2c), (3a), and (3b), Fig. 5 shows the results from an analytical calculation of the shock front propagation and the expansion following shock breakout. These results compare reasonably well with the results from the corresponding 2D hydrodynamic simulation and will be used in Sec. IV D to estimate the shape of the deformed target foil and the direction of the accelerated proton beam.

III. EXPERIMENTAL METHOD

The experiments are performed with the 10 Hz multiterawatt femtosecond laser at the Lund Laser Centre. It is a Ti:sapphire system, operating at 800 nm, capable of delivering 35 fs pulses of up to 30 TW on target. The system is

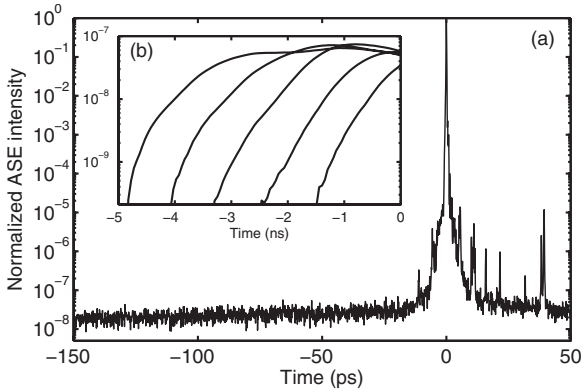

FIG. 6. (a) High dynamic range third order autocorrelation measurement of the laser pulse profile. On this time scale, the laser intensity is constant until it starts to rise 15 ps before the main pulse. The ASE pedestal intensity is measured 100 ps before the main pulse. (b) The ASE pedestal duration is controlled by selecting the timing of the gating Pockels cells relative to the main laser pulse. The photodiode measurements have been normalized to corresponding third order autocorrelations.

based on chirped pulse amplification and incorporates a regenerative amplifier for preamplification and two multipass amplifiers. The regenerative preamplifier has a gain of almost 10^8 and special caution is devoted to the optimization of this amplifier on a day-to-day basis in order to minimize the ASE intensity of the compressed pulses to around 10^{-8} of the main pulse peak intensity.

A. Control of amplified spontaneous emission

The temporal pulse shape is diagnosed on a picosecond time scale by a high dynamic range third order autocorrelator (Sequoia, Amplitude Technologies). A typical temporal profile is shown in Fig. 6(a). On this time scale, the laser intensity is reasonably constant until it starts rising 15 ps before the main pulse. Consequently, we quote the ASE intensity as the intensity in the flat part of this pedestal, as measured 100 ps before the main pulse.

The ASE pedestal is diagnosed on a nanosecond time scale by a fast photodiode and a high bandwith oscilloscope. Three synchronized pulse cleaning Pockels cells, each of which has a rise time of 1.0 ns, are incorporated in the system. Figure 6(b) shows the ASE pedestal for different timing of these optical gates relative to the main pulse. The photodiode measurements are normalized to simultaneous third order autocorrelations. On a nanosecond time scale, the ASE intensity closely follows the opening of the Pockels cells. Hereafter, we refer to the ASE duration as the time between the half maximum of the rising edge of the ASE pedestal and the peak of the main pulse.

The contrast ratio between the main pulse intensity and the ASE intensity is highly dependent on the energy that seeds the regenerative amplifier. The laser system incorporates an acousto-optic programmable dispersive filter (Dazzler, Fastlite). This device, positioned at the oscillator output, is normally used to precompensate for high order dispersion and gain narrowing in the amplifier chain, but it

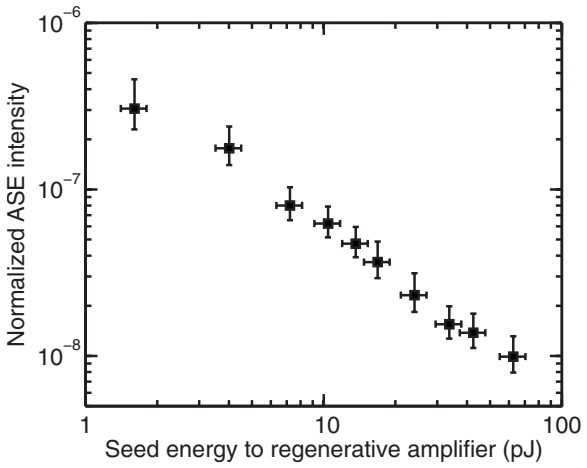

FIG. 7. By controlling the seed energy to the regenerative amplifier, it is possible to control the ASE intensity of the amplified laser pulse.

can also be used as a programmable attenuator in order to control the seed energy to the regenerative amplifier via the filter control software. Figure 7 shows the dependence of the ASE intensity on the seed energy to the regenerative amplifier. This method for adjusting of the ASE intensity does not affect the main pulse duration or the energy.

B. Experimental arrangement

A schematic of the experimental setup is shown in Fig. 8. In this study, pulses with a total energy of 700 mJ, a duration of 35 fs [full width at half maximum (FWHM)], and a 50 mm diameter enter the vacuum target chamber. The laser beam is focused by an $f/3$ off-axis parabolic mirror to an 8 μm (FWHM) focal spot, giving an inferred peak intensity of 2×10^{19} W/cm^2. Target foils of different materials and thicknesses are positioned in the focal plane for p-polarized

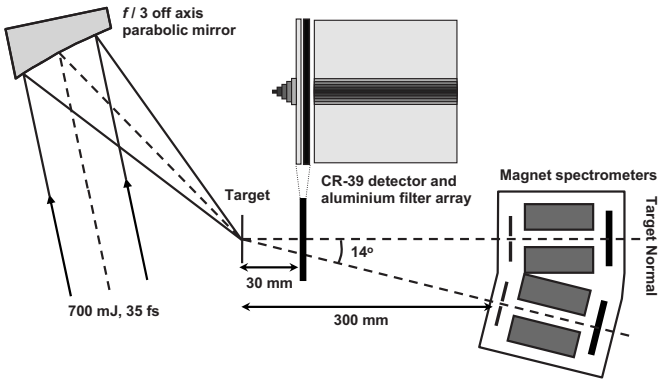

FIG. 8. Schematic of the experimental arrangement showing the geometry and the proton diagnostics. The laser is focused by an $f/3$ off axis parabola onto a thin foil target. A filter mask consisting of stripes of Al foil of different thicknesses enables measurement of the spatial profile above chosen threshold proton energies. Alternatively, two magnetic spectrometers register the proton energy spectrum along the target normal direction and at 14° toward the laser axis.

irradiation at a 45° angle of incidence. The target holder can be loaded with up to 50 individual foil targets.

C. Target positioning system

Prior to each full power shot, the intensity distribution of a collinear alignment beam, reflected off the target surface, is captured by an imaging system as a function of the longitudinal position of the target foil. Irregularities on the target foil surface produce speckles in the reflected beam. The speckle size is determined through Fourier image analysis and the target position that produces the largest speckles, i.e., the focal position, is found through a polynomial fit to the calculated values. The acquisition and analysis are fully automated and controlled from a LABVIEW interface. The system facilitates reproducible positioning of solid targets in the focal plane to within a Rayleigh range. An additional feature of this positioning system is that it provides information on the local surface orientation of each individual target through the direction of the reflected alignment beam. This allows the angle of incidence to be adjusted to be exactly the same for each shot.

D. Proton beam diagnostics

In order to diagnose the proton beam, we use CR39 nuclear track detectors, sensitive to protons and ions but insensitive to electrons and x rays [24]. The spatial distribution is captured by a 50×50 mm plate of CR39, positioned 30 mm from the target. A filter mask, consisting of stripes of aluminum with different thickness, is placed directly in front of the detector plate. This enables simultaneous measurement of the spatial distribution of protons above different threshold energies. A feeding mechanism allows up to 20 consecutive shots to be recorded on different detector plates before the vacuum chamber must be opened and the detectors replaced. Alternatively, when the plate feeder is removed, the energy spectrum can be registered on CR39 detectors behind two compact magnetic spectrometers, positioned 300 mm from the target, in the target normal direction and at 14° toward the laser axis.

IV. EXPERIMENTAL RESULTS AND DISCUSSION

Under conditions where the ASE has no influence on the rear target surface, we obtain a well defined proton beam with a continuous energy spectrum extending up to a few MeV; see Figs. 9(a) and 9(b). The beam is centered on the target normal axis and has a divergence that decreases with increasing energy.

A. Influence of shock waves

Figures 9(c) and 9(d) show the energy spectrum and spatial distribution of proton beams, accelerated under conditions where an ASE-driven shock wave strongly influences the shape of the rear surface. The beam is significantly shifted toward the laser direction with a deflection angle that increases with proton energy.

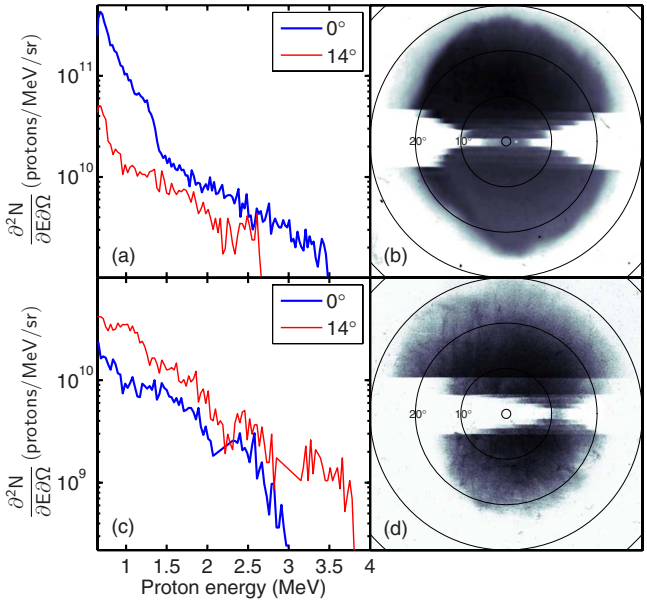

FIG. 9. (Color online) [(a),(c)] Energy spectra and [(b),(d)] spatial distributions of proton beams obtained using 6 μm Al foils. In (a) and (b), the ASE has no influence on the rear surface (τ_{ASE} =0.5 ns, $I_{ASE}=2\times10^{11}$ W/cm^2) and the most energetic protons are emitted along the target normal. In (c) and (d), the amount of ASE has been increased (τ_{ASE}=1.5 ns, $I_{ASE}=2\times10^{12}$ W/cm^2) and the most energetic protons are shifted toward the laser axis. The filter arrays in (b) and (d) are different and correspond to a maximum cutoff energy of 2.8 MeV and 4.8 MeV, respectively.

The phenomenon may be explained by considering the effects of an ASE-driven shock wave in combination with the oblique incidence of the main laser pulse; see Fig. 10. Given an ASE pedestal of sufficient intensity and duration, the initially planar target is deformed into a convex profile before the main pulse arrives. The main laser pulse, incident at 45°, accelerates electrons according to a number of different mechanisms. The relative importance of these mechanisms varies with the laser intensity and the preplasma conditions. At low intensities and steep plasma gradients, resonance absorption dominates and electrons are accelerated predominantly along the target normal, whereas at high intensities and long plasma scale lengths, electrons are accelerated primarily in the laser direction [25]. Other experiments have confirmed that, under our experimental conditions, two populations of hot electrons are created [26] and that the most energetic population, heated by the $v\times B$ force of the intense laser field, is directed along the laser direction.

When the electrons reach the rear surface, they are asymmetrically distributed over the deformation. In particular, the most energetic electrons appear in an area of the target where the local target normal points away from the global target normal. Hence the direction of the strongest electric field is also shifted and the most energetic protons are steered toward the laser axis. Low energy protons are emitted from a much larger area [2], so for these the deformation has a defocusing effect rather than a steering effect.

The proton beam in Fig. 9(d) is significantly influenced by the ASE-driven shock, but has a well defined structure. The most energetic protons (>4.8 MeV) are shifted by 13° but are still emitted within a 4° cone. To produce a high energy proton beam with a good beam quality, such as the examples in Figs. 9(b) and 9(d), requires an initially cold emitting surface at the time the hot electrons are created. Not illustrated here is the fact that increasing the ASE intensity or duration beyond certain limits locally disrupts the target, producing an inferior beam quality or even terminating the proton emission altogether.

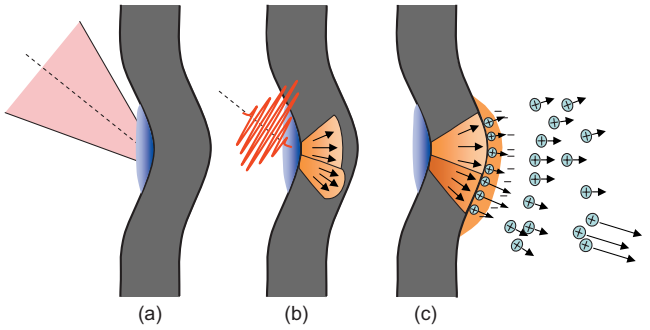

FIG. 10. (Color online) Sequential illustration of proton acceleration in a shocked target. (a) Prior to the main pulse arrival, the ablation pressure induced by the ASE deforms the target foil. (b) The main pulse arrives under oblique incidence and generates a population of hot electrons. (c) The most energetic electrons traverse the target and set up a strong electric field in an area where the local target normal is shifted toward the laser axis, away from the global target normal. Consequently, during the plasma expansion, the most energetic protons are accelerated in a direction that is shifted toward the laser axis, with an angle that increases with the magnitude of the local deformation.

B. Influence of target properties

Next, the influence of the target material and thickness on the magnitude of the proton deflection is investigated. Keeping the laser properties constant, the thickness of aluminum and copper target foils is varied; see Fig. 11. For a laser contrast ratio of 1×10^7, the inferred ASE intensity is 2×10^{12} W/cm^2. At this intensity, the shock velocity is estimated to be 9 μm/ns in Al and 6 μm/ns in Cu. For a 1 ns long ASE pedestal, the shock has not yet reached the rear surface of 12 μm foils when the main pulse arrives and, consequently, no proton beam deflection is observed for either Cu or Al foils. For the 6 μm foils, the shock has reached the rear surface of both the Cu and Al foils before the main pulse arrives. After shock breakout, the rear surface expands with a velocity of 5 μm/ns in Al and 3 μm/ns in Cu. This means that the 6 μm Al foil is deformed by 2 μm and indeed we observe the onset of an energy dependent proton beam emission. However, for 6 μm Cu, we observe only a very small deflection since, even though the shock breaks through, there is no time for expansion before the main pulse arrives. Finally, for the 3 μm foils, the Al foil is deformed by 3 μm, giving an even larger deflection than the 6 μm Al foil. The 3 μm Cu foil is deformed by 1.5 μm, giving a deflection slightly smaller than the 6 μm Al foil. In conclusion, beams emitted from thinner foils are more de-

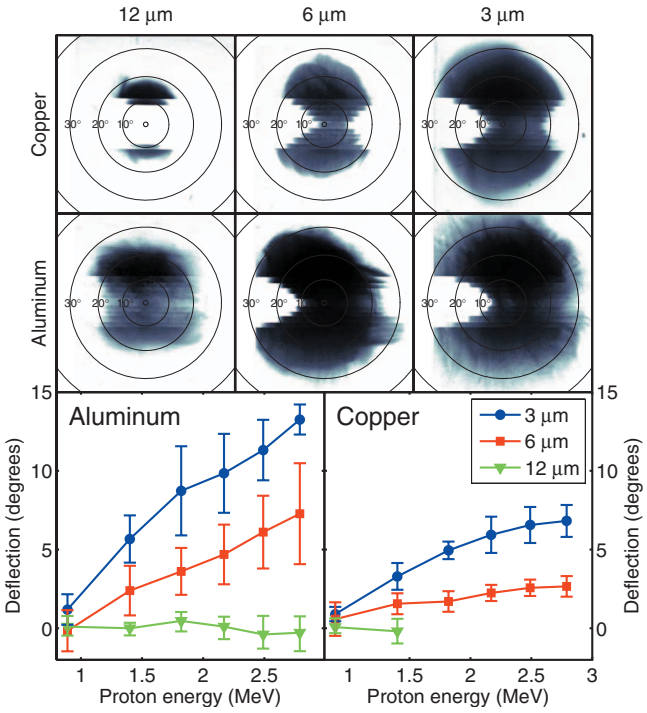

FIG. 11. (Color online) Influence of the target properties on the energy dependent emission direction. The ASE pedestal intensity and duration is 2×10^{12} W/cm^2 and 1 ns, respectively. The panels in the top and middle rows show representative proton beams, obtained from Al and Cu foils of different thicknesses. The complete data set is compiled in the two bottom diagrams, where the error bars denote the standard deviation taken over three consecutive shots.

flected since they have more time to expand after breakout. Beams emitted from Al foils are more deflected than beams emitted from the denser Cu foils because of the difference in shock and expansion velocity.

C. Influence of ASE pedestal properties

The onset of an energy dependent proton emission direction depends on the relation between the target thickness, the shock velocity, and the ASE pedestal duration. In turn, the shock velocity is determined by the ASE intensity through Eqs. (1), (3a), and (3b). For a given thickness, a skewed proton beam can be obtained by either increasing the ASE pedestal duration or the intensity. Figure 12 shows data from three representative shots on 6 μm Al for three different ASE conditions. First, the contrast ratio is set to 3×10^7, giving an inferred shock driving intensity of 6×10^{11} W/cm^2. In Al, the corresponding shock and expansion velocities are 7 μm/ns and 3 μm/ns, respectively. For a short, 1 ns pedestal, we get a maximum deformation of 0.4 μm yielding a very small or no proton beam deflection. However, increasing the ASE duration to 2 ns gives a calculated deformation of 3 μm and a significant beam deflection. Increasing the inferred ASE intensity to 4×10^{12} W/cm^2 gives a calculated shock velocity of 10 μm/ns and an expansion velocity of 7 μm/ns. A 1 ns ASE pedestal at this increased intensity should therefore also produce a 3 μm

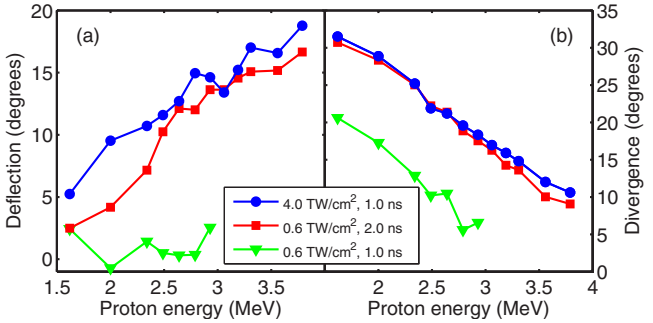

FIG. 12. (Color online) Influence of the ASE intensity and duration on (a) the energy dependent proton beam deflection toward the laser axis and (b) on the half apex angle of the emission cone.

maximum deformation. Indeed, as shown in Fig. 12(a), the intense but short pedestal generates a proton beam deflection of magnitude similar to the weak but long pedestal.

Closely correlated with the onset of an energy dependent proton emission direction is an increase in beam divergence. As shown in Fig. 12(b), increasing the ASE duration or intensity produces a proton beam with significantly larger divergence. This phenomenon can also be observed in the representative examples in Fig. 11, where the target thickness is decreased. The increased divergence could be interpreted as resulting from the breakout of an ASE-driven shock wave. It has been shown in simulations and in experiments that a concave rear surface acts to focus the emitted proton beam [27,28]. In the same way, a convex rear surface, produced by the breakout of a shock, could be expected to defocus the proton beam, thereby increasing the beam divergence.

D. Prediction of the emission direction

The proton beam deflection angle is directly related to the lateral and longitudinal extent of the foil deformation. The longitudinal extent is determined by the expansion velocity and the time available for the expansion, while the lateral extent is determined by the size of the focal spot. To probe the dynamics of the foil deformation the pulse contrast is set to 1×10^8, giving an inferred ASE intensity of 2×10^{11} W/cm^2. Using a single layer Al filter in front of the CR39 detector plate, the emission direction of protons above 2.5 MeV from 6 μm Al foils is measured as a function of the ASE duration. As shown in Fig. 13, the proton beam is emitted along the target normal, until the shock breaks through the rear surface. After this point, the beam is steered away from the target normal with an angle that increases with increasing pedestal duration. Also shown in Fig. 13 is the time dependent deflection angle for proton beams produced in 6 μm Cu targets. As expected, the shock appears to break out at a later time and, after that point, the deflection angle increases at a slower rate than for the Al foil. These observations are consistent with slower shock and expansion velocities in Cu as compared to Al.

In order to do a quantitative prediction of the beam deflection angle, we estimate the shape of the rear surface using the model described in Sec. II C. The inset in Fig. 13 shows the calculated shape for a 2.0 ns long ASE pedestal with an

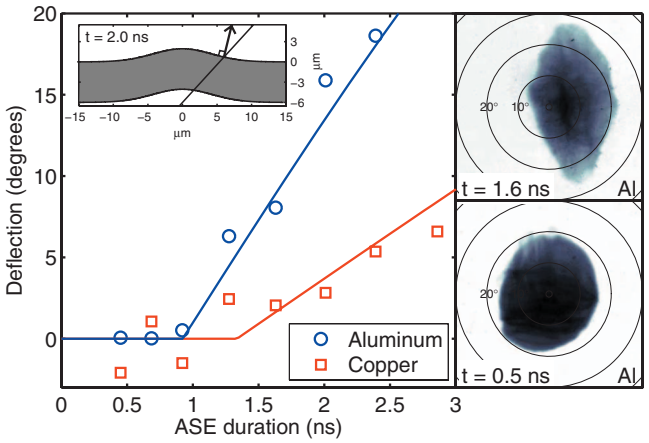

FIG. 13. (Color online) Proton beam deflection toward the laser axis as a function of ASE duration. The target is 6 μm Al and Cu and the inferred ASE intensity is 2×10^{11} W/cm^2. As shown in the bottom right panel, the proton beam stays on the target normal axis for the shortest ASE pedestal. After shock breakout, the proton beam is steered toward the laser axis as shown in the top right panel. The inset shows the calculated shape of the foil for a 2.0 ns long ASE pedestal. The modeled emission direction (solid lines) is the calculated target normal direction at the point where the laser axis intersects the rear surface.

intensity of 2×10^{11} W/cm^2. The proton emission direction is calculated as the direction of the local target normal where the laser axis, incident at 45°, intersects the rear surface. In this model, we have only one free parameter: the ASE intensity distribution. With the peak ASE intensity fixed at 2×10^{11} W/cm^2, we assume a Gaussian intensity distribution and fit the width of this function to the Al data set. This gives an inferred ASE spot diameter of 8 μm (FWHM), the same as the measured spot size. Keeping the parameters of the ASE we change only the material constants (ρ_0, c_0, and α) and apply the model to the Cu data set. This gives excellent agreement with the experimental observations, as shown in Fig. 13.

V. CONCLUSION

We have demonstrated the possibility of using the intrinsic ASE pedestal to shape a thin foil and thereby control the proton emission angle. A natural extension to this work is to increase the contrast ratio of the laser to a level where the ASE has only a minor effect and instead use a secondary, independently configurable, laser pulse in order to shape the target and thereby optically control the proton emission. It is, for example, conceivable that, by using a ring-shaped steering pulse, it would be possible to control not only the direction but also the divergence of the proton beam. This could open interesting prospects for future high repetition rate laser-based proton accelerators.

We acknowledge support from the Swedish Research Council, the Knut and Alice Wallenberg Foundation, and the EU Access to Research Infrastructures Programme (RII3-CT-2003-506350 Laserlab Europe).

[1] D. Neely *et al.*, Appl. Phys. Lett. **89**, 021502 (2006).
[2] T. E. Cowan *et al.*, Phys. Rev. Lett. **92**, 204801 (2004).
[3] M. Borghesi, A. J. MacKinnon, D. H. Campbell, D. G. Hicks, S. Kar, P. K. Patel, D. Price, L. Romagnani, A. Schiavi, and O. Willi, Phys. Rev. Lett. **92**, 055003 (2004).
[4] S. V. Bulanov and V. S. Khoroshkov, Plasma Phys. Rep. **28**, 453 (2002).
[5] K. W. D. Ledingham *et al.*, J. Phys. D **37**, 2341 (2004).
[6] K. Krushelnick *et al.*, IEEE Trans. Plasma Sci. **28**, 1184 (2000).
[7] T. Grismayer and P. Mora, Phys. Plasmas **13**, 032103 (2006).
[8] A. J. Mackinnon, M. Borghesi, S. Hatchett, M. H. Key, P. K. Patel, H. Campbell, A. Schiavi, R. Snavely, S. C. Wilks, and O. Willi, Phys. Rev. Lett. **86**, 1769 (2001).
[9] M. Allen, P. K. Patel, A. Mackinnon, D. Price, S. Wilks, and E. Morse, Phys. Rev. Lett. **93**, 265004 (2004).
[10] F. Lindau, O. Lundh, A. Persson, P. McKenna, K. Osvay, D. Batani, and C. G. Wahlström, Phys. Rev. Lett. **95**, 175002 (2005).
[11] P. McKenna *et al.*, Philos. Trans. R. Soc. London, Ser. A **364**, 711 (2006).
[12] M. Kaluza, J. Schreiber, M. I. K. Santala, G. D. Tsakiris, K. Eidmann, J. Meyer-ter-Vehn, and K. J. Witte, Phys. Rev. Lett. **93**, 045003 (2004).
[13] M. H. Xu *et al.*, Phys. Plasmas **13**, 104507 (2006).
[14] R. Ramis, R. Schmalz, and J. Meyer-Ter-Vehn, Comput. Phys. Commun. **49**, 475 (1988).
[15] D. C. Swift, T. E. Tierney IV, R. A. Kopp, and J. T. Gammel, Phys. Rev. E **69**, 036406 (2004).
[16] J. Lindl, Phys. Plasmas **2**, 3933 (1995).
[17] *LASL Shock Hugoniot Data*, edited by S. P. Marsh (University of California Press, Berkeley, 1980).
[18] S. Eliezer, Plasma Phys. Controlled Fusion **45**, 181 (2003).
[19] C. Dai, H. Tan, and H. Geng, J. Appl. Phys. **92**, 5019 (2002).
[20] J. H. Nguyen and N. C. Holmes, Nature (London) **427**, 339 (2004).
[21] J.-W. Jeong and K. J. Chang, J. Phys.: Condens. Matter **11**, 3799 (1999).
[22] M. Werdiger *et al.*, Laser Part. Beams **17**, 547 (1999).
[23] C. W. Greeff and M. J. Graf, Phys. Rev. B **69**, 054107 (2004).
[24] F. H. Seguin *et al.*, Rev. Sci. Instrum. **74**, 975 (2003).
[25] M. I. K. Santala *et al.*, Phys. Rev. Lett. **84**, 1459 (2000).
[26] F. Brandl *et al.*, Europhys. Lett. **61**, 632 (2003).
[27] S. C. Wilks *et al.*, Phys. Plasmas **8**, 542 (2001).
[28] P. K. Patel, A. J. Mackinnon, M. H. Key, T. E. Cowan, M. E. Foord, M. Allen, D. F. Price, H. Ruhl, P. T. Springer, and R. Stephens, Phys. Rev. Lett. **91**, 125004 (2003).